Paleoceanography and Paleoclimatology

RESEARCH ARTICLE
10.1029/2025PA005388

Evidence for Limited Atmospheric CO_2 Rise at the Miocene Climatic Optimum

Evi Wubben[1], Joost Frieling[1,2,3], Yannick F. Bats[1], Linda van Roij[1], Kirsten de Haan[1], Gert-Jan Reichart[1,4], Francien Peterse[1], Francesca Sangiorgi[1], Marcel T. J. van der Meer[4], and Appy Sluijs[1]

[1]Department of Earth Sciences, Faculty of Geosciences, Utrecht University, Utrecht, the Netherlands, [2]Department of Earth Sciences, University of Oxford, Oxford, UK, [3]Department of Geology, Ghent University, Ghent, Belgium, [4]NIOZ Royal Netherlands Institute for Sea Research, Den Burg, the Netherlands

Key Points:

- Bulk organic carbon, alkenones and dinocysts show a small rise in phytoplankton ^{13}C-fractionation during the Miocene Climatic Optimum (MCO)
- Based on bootstrapping culture and surface sediment data, we estimate CO_2 based on alkenone ^{13}C-fractionation
- These and published records suggest MCO CO_2 was 100–150 µatm higher than the preceding interval

Supporting Information:

Supporting Information may be found in the online version of this article.

Correspondence to:

A. Sluijs,
A.Sluijs@uu.nl

Citation:

Wubben, E., Frieling, J., Bats, Y. F., van Roij, L., Haan, de. K., Reichart, G.-J., et al. (2026). Evidence for limited atmospheric CO_2 rise at the Miocene Climatic Optimum. *Paleoceanography and Paleoclimatology*, *41*, e2025PA005388. https://doi.org/10.1029/2025PA005388

Received 8 DEC 2025
Accepted 26 MAY 2026

Author Contributions:

Conceptualization: Evi Wubben, Appy Sluijs
Formal analysis: Evi Wubben, Yannick F. Bats
Funding acquisition: Appy Sluijs
Investigation: Evi Wubben, Joost Frieling, Yannick F. Bats, Linda van Roij, Kirsten de Haan, Marcel T. J. van der Meer
Methodology: Yannick F. Bats, Linda van Roij
Project administration: Appy Sluijs
Supervision: Francien Peterse, Francesca Sangiorgi, Appy Sluijs

Abstract The Miocene Climatic Optimum (MCO; 16.9–14.7 Ma) was a relatively warm period with atmospheric CO_2 averaging ~500 µatm but CO_2 change across its onset is poorly documented. We present a record of algal ^{13}C-fractionation covering the Early to Middle Miocene (~18.5–15 Ma), with a gap at the MCO onset, from Ocean Drilling Program Site 959 in the tropical Atlantic. Bulk marine organic carbon, alkenones and the dinoflagellate cyst species *Spiniferites ramosus* all show higher ^{13}C-fractionation within the MCO than in the interval below the MCO. Based on various models to convert this signal to CO_2, including a new statistical model based on core top and culture data, these records imply a CO_2 rise of ~100–150 µatm across the MCO onset, consistent with previously published information.

Plain Language Summary The Miocene Climatic Optimum (MCO), between about 17 and 15 million years ago, was a relatively warm period in Earth history. This warming was thought to originate from a rise in the CO_2 concentration in the atmosphere that intensified the greenhouse effect. However, knowledge of CO_2 concentrations across this time interval was not sufficient to test this hypothesis. We reconstruct atmospheric CO_2 concentrations across this period by analyzing the chemistry of fossil remains of algae, which is CO_2-sensitive. This information shows that CO_2 concentrations only rose by a modest amount when the MCO started.

1. Introduction

Global climate during the Miocene Climatic Optimum (MCO; ~16.9–14.7 Ma) was ~7–8°C warmer than present-day (Steinthorsdottir, Coxall, et al., 2021). This warmth is typically explained by mean atmospheric CO_2 levels of 500 µatm, with peaks up to ~1,000 µatm (Sosdian et al., 2018; Steinthorsdottir, Jardine, & Rember, 2021; Super et al., 2018). As such, the MCO is of particular interest as a future climate analogue because the continental configuration, vegetation and cryosphere were more similar to the present-day than more distant high-CO_2 analogs such as the Eocene (Steinthorsdottir, Coxall, et al., 2021).

The onset of the MCO is marked by an ~1.0‰ drop in deep ocean benthic foraminifer oxygen isotope ratios ($\delta^{18}O_{benthic}$). To what extent $\delta^{18}O$ change represents warming and/or ice sheet loss (Holbourn et al., 2015; Woodruff & Savin, 1991) remains uncertain. Stable carbon isotope ratios of benthic foraminifera ($\delta^{13}C_{benthic}$) exhibit a positive excursion following the MCO onset, termed "Monterey," presumably associated with excess organic carbon burial (Holbourn et al., 2015; Sosdian et al., 2020; Vincent & Berger, 1985). Across the MCO, $\delta^{13}C_{benthic}$, $\delta^{18}O_{benthic}$ and high-resolution sea surface temperature (SST) records reveal prominent orbital cyclicity, notably eccentricity (Holbourn et al., 2007; Wubben et al., 2024). This includes orbitally-forced variability in the carbon cycle (Holbourn et al., 2015; Woodruff & Savin, 1991), climate and monsoon (Sosdian et al., 2020; Spiering et al., 2024; Wubben et al., 2024), including an apparent interval of "peak warmth" at ~15.6 Ma (Holbourn et al., 2015; Wubben et al., 2024).

Despite the generally assumed role for CO_2 in MCO warming (e.g., Herbert et al., 2022; Kasbohm et al., 2023; Kasbohm & Schoene, 2018), available CO_2 reconstructions (Greenop et al., 2014; Sosdian et al., 2018, 2020) are not continuous across the MCO onset. Most records have been generated to assess pCO_2 change during the MCO or across its termination (Badger et al., 2013; Greenop et al., 2014; Sosdian et al., 2020) rather than to evaluate pCO_2 change associated with the start of the MCO. The latest compilation of data, derived from various types of

Visualization: Evi Wubben, Yannick F. Bats
Writing – original draft: Evi Wubben
Writing – review & editing: Evi Wubben, Joost Frieling, Yannick F. Bats, Gert-Jan Reichart, Francien Peterse, Marcel T. J. van der Meer, Appy Sluijs

proxy records from multiple locations, suggest that CO_2 concentrations during the MCO were higher than before by on average perhaps 150 µatm (CenCO$_2$PIP Consortium, 2023). However, the timing of this CO_2 rise and its relation to the onset of the MCO as defined in $\delta^{18}O_{benthic}$ records is unclear, and CO_2 variability within the MCO seems larger than the overall magnitude of the rise (Greenop et al., 2014; Sosdian et al., 2020).

We apply a set of proxies based on the [$CO_{2(aq)}$]-dependency of phytoplankton ^{13}C-fractionation (ε_p) to add to the relative scarcity of data in this important time interval. Both culture experiments and surface sediment data suggest that CO_2 concentration is a major factor driving ^{13}C-fractionation in these sedimentary phases, although the relation is strongly impacted by (species specific) confounding factors (e.g., Arthur et al., 1985; Brandenburg et al., 2022; Hoins et al., 2016; Phelps, Stoll, et al., 2021). The traditional assumption in CO_2-paleobarometry based on algal ^{13}C-fractionation, using biomarkers (e.g., alkenones, phytane) or bulk marine organic matter as substrates, is that algae take up inorganic carbon via diffusion of dissolved CO_2 and that higher [$CO_{2(aq)}$] causes increased ^{13}C-fractionation (Freeman & Hayes, 1992; Naafs et al., 2016; Pagani, 2002; Witkowski et al., 2018; Zhang et al., 2013). However, this assumption is complicated by several environmental and physiological factors associated with carbon acquisition, such as an influence of light regime and the active HCO_3^- uptake ability by most algal types, including the haptophytes that produce alkenones that are often used for CO_2 reconstructions (Badger et al., 2019; Phelps, Stoll, et al., 2021; Rost et al., 2002; Rost, Riebesell, & Sültemeyer, 2006; Stoll et al., 2019). Also dinoflagellates use both CO_2 and HCO_3^- as a carbon source (Burkhardt et al., 1999a; Rost, Richter, et al., 2006). In the species we use, *Gonyaulax spinifera*, CO_2-dependent ^{13}C-fractionation (up to 800 µatm in dilute batch experiments) is quantitatively consistent with proportions of acquired CO_2 relative to HCO_3^- (Hoins et al., 2016).

To overcome such physiological and environmental issues, Stoll et al. (2019) applied a multiple linear regression analysis on haptophyte ε_p culture data, which consisted of light availability, [$CO_{2\ (aq)}$], growth rate and cell size as independent variables. These variables are shown to have a significant effect on ε_p values, which implies they must be independently constrained for CO_2 reconstructions using this regression model. Cell size can be constrained using coccolith size measurements. However, assumptions must be made for growth rate and light availability, and this is not straightforward in the paleodomain.

We present phytoplankton ^{13}C-fractionation recorded in alkenones produced by haptophytes, bulk marine organic carbon, and the dinoflagellate cyst (dinocyst) species *Spiniferites ramosus* (produced by extent phototrophic *Gonyaulax spinifera*) preserved in sediments recovered at Ocean Drilling Program (ODP) Site 959 in the eastern equatorial Atlantic. By applying a multi substrate approach we limit the impact of individual species-specific fractionation effects on CO_2 reconstructions. Moreover, we devise a new pragmatic non-parametric approach to explore proxy uncertainty using bootstrapping of CO_2 and ^{13}C fractionation values from both surface sediment and culture data for alkenone paleobarometry. Importantly, oceanographic variability across the MCO at Site 959 has been well constrained in previous work (Spiering et al., 2024; Wubben et al., 2023, 2024) which allows us to assess local factors other than CO_2 that might have affected ^{13}C-fractionation. Ultimately, we use the records and a sensitivity study to test the influence of various assumptions to estimate a range of plausible CO_2 changes across the MCO.

2. Materials

Lower to Middle Miocene pelagic, biogenic sediments (~18.2–15 Ma) at ODP Site 959 in the eastern equatorial Atlantic (3°37.659′N, 2°44.112′W) consist of diatom-rich nannofossil chalk and clayey diatomites with minor amounts of aeolian material (Wubben et al., 2023). Geochemical and lithological records exhibit pronounced precession to eccentricity-cycles, that provided the basis for an orbitally tuned age-depth model that includes a hiatus just before the base of the MCO (Spiering et al., 2024; Wubben et al., 2023, 2024). The presence and duration of this hiatus may be subject of discussion (Wubben et al., 2023), but in any case the section allows for proper comparison between pre-MCO and MCO conditions. TEX_{86} paleothermometry shows a ~2°C rise in SST across the MCO onset (~16.9 Ma), as well as strong orbital variability throughout the MCO (Wubben et al., 2024). The orbital SST variability at least partly relates to upwelling driven by West African Monsoon dynamics, reflected in biogenic Ba (Ba_{bio}) peaks and enhanced dust influx (i.e., elevated Ti/Al ratios) (Wubben et al., 2024). During periods of strong upwelling surface waters were likely not in equilibrium with atmospheric CO_2. However, these local oceanographic factors can be isolated from atmospheric CO_2 trends as Early and

Middle Miocene orbital-scale monsoon-driven upwelling intensity is well constrained at this site (Spiering et al., 2024; Wubben et al., 2024).

3. Methods

3.1. Approach

3.1.1. Substrates for ε_p Assessment

We apply methods that utilize relationships between [$CO_{2(aq)}$] and ^{13}C-fractionation (ε_p) in phytoplankton. First, we assess ε_p based on the $\delta^{13}C$ of long-chain alkenones produced by haptophyte algae in the surface mixed layer ($\delta^{13}C_{37:2}$) ($n = 18$, average resolution: ~150 kyr). We also assess orbital-scale ε_p variability by generating a high resolution $\delta^{13}C$ record of bulk sediment total organic carbon ($\delta^{13}C_{TOC}$) ($n = 146$, average resolution = 16 kyr). The bulk organic matter at Site 959 predominantly derives from marine primary producers, based on overall sediment composition, palynological and biomarker data (Wubben et al., 2023, 2024). Variability in $\delta^{13}C_{TOC}$ may result from varying organic matter sources (phytoplankton groups or sourcing from higher trophic levels), which we evaluate by comparing it to the more specific alkenone record.

We also present ε_p data based on the organic dinocyst species *Spiniferites ramosus* ($\varepsilon_{p(dino)}$, $n = 11$, average resolution = 330 kyr), produced by the autotrophic extant dinoflagellate *Gonyaulax spinifera*. Carbon isotope signatures of dinoflagellates ($\delta^{13}C_{dino}$) are retained in their cysts (Sluijs et al., 2018) and sediment surface analyses show that $\varepsilon_{p(dino)}$ relates to surface ocean pCO_2 (Frieling et al., 2023). Although the *Gonyaulax spinifera* ε_p—pCO_2 relation has been quantified (Hoins et al., 2015), it is unclear how this translates to its cyst *S. ramosus*.

To assess the $\delta^{13}C$ values of dissolved inorganic carbon (DIC) from which the organic phases are synthesized and determine ε_p, we use the published bulk carbonate $\delta^{13}C$ values generated on the same samples (Wubben et al., 2023). The bulk carbonate at Site 959 dominantly represents calcareous nannofossils. Although—to our knowledge—not documented in detail for the Miocene, differences in ^{13}C-fractionation between DIC and various calcareous nannofossil species are relatively small in published records (Bolton & Stoll, 2013; Stoll, 2005). Consequently, bulk carbonate—even more so than planktonic foraminifer records that may suffer from calcification depth variations—is a good proxy for $\delta^{13}C_{DIC}$ variability (Reghellin et al., 2015).

3.1.2. Relationships Between ε_p and [CO_2]

In the CO_2 diffusion model, ε_p and CO_2 from the $\delta^{13}C$ values are related using the widely applied approach of Jasper and Hayes (1990),

$$\varepsilon_p = \varepsilon_f - \frac{b}{[CO_{2(aq)}]}$$

where ε_f is the ^{13}C-fractionation that occurs during RubisCO carboxylation (25‰), and b represents the sum of physiological factors (e.g., growth rate, cell geometry) that impact fractionation. Seawater phosphate concentrations are used as a proxy for b (cf., Zhang et al., 2013) and we explore a likely range between 0.05 and 1.5 µmol/kg and propagate uncertainty in our estimates (see raw data and calculations in the supplemental information). We use published TEX_{86}-based temperature estimates (Wubben et al., 2024) for calculations of carbonate chemistry. Atmospheric CO_2 concentration is determined with Henry's Law assuming constant sea-air gas exchange (see supplementary text for detailed methodology).

To properly take uncertainty of the ε_p-[$CO_{2\ (aq)}$] relationship into account, an additional non-parametric approach is applied to calculated alkenone ε_p values, which assumes no underlying relationship between ε_p and [$CO_{2\ (aq)}$]. The approach is based on bootstrapping ($n = 1{,}000$) pCO_2 and alkenone ε_p values from culture experiments on the alkenone producing haptophytes *Gephyrocapsa huxleyi* and *G. oceanica* (Figure S1 in Supporting Information S1) (Bidigare et al., 1997; McClelland et al., 2017; Pearson et al., 2025; Phelps, Hennon, et al., 2021; Riebesell et al., 2000; Rost et al., 2002) or from a compilation of alkenone data from core-tops and sediment traps, hereafter referred to as the core top data; Figure S2 in Supporting Information S1 (Phelps, Stoll, et al., 2021). The culture data are used because these taxa are the modern producers of alkenones in open ocean environments and therefore the best possible representation for Miocene alkenone synthesizing coccolithophores. In R, the

distributions of [$CO_{2\ (aq)}$] values for which culture or core-top ε_p values equal the Miocene sedimentary alkenone ε_p values are bootstrapped, which consists of resampling with replacement, determining mean [$CO_{2\ (aq)}$], and repeating this n times. The distributions of bootstrapped estimates of mean [$CO_{2\ (aq)}$] values are converted to distributions of pCO_2 according to Henry's law.

Considering the average uncertainty of core top alkenone $\delta^{13}C$ measurements is 0.31‰ (Phelps, Stoll, et al., 2021), and the average uncertainty in bulk carbonate $\delta^{13}C$ measurements is 0.07‰ (Wubben et al., 2023), we use $2 \times 0.32‰$ ($\sqrt{[0.31^2 + 0.07^2]} = 0.32$) as the ε_p tolerance for bootstrapped distributions, which represents the 95% CI of the sedimentary ε_p measurements. Considering temperature substantially forces ε_p values (Figure S2 in Supporting Information S1) (Phelps, Stoll, et al., 2021), only core top ε_p values for which temperatures are within a 5°C range of the TEX_{86}-based paleotemperature estimates are used for bootstrapping. For the bootstrapping of culture data (Figure S1 in Supporting Information S1) we did not apply any temperature constraint because culture temperatures are restricted to a range of 15–18°C. Additionally, considering cultures have such a limited temperature range, the core-top and culture bootstraps are treated as two separate methods and therefore performed and presented independently. To account for asymmetric variability, we plot bootstrapped pCO_2 values as boxplots.

Collectively, the bootstrap workflow to reconstruct pCO_2 comprises of the following steps:

1. Inverse matching to observations: For each alkenone-derived ε_p measurement ($\varepsilon_{p\text{-meas}}$), all [$CO_{2\ (aq)}$] values for which $\varepsilon_{p\text{-meas}}$ matches ε_p values from culture or core-top measurements within a tolerance of ±0.64‰ (=2σ combined analytical uncertainty) are extracted, subject to independent constraints on temperature (i.e., TEX_{86}-derived SSTs).
2. Statistical summarization: The distributions of extracted [$CO_{2\ (aq)}$] values—corresponding to each alkenone ε_p measurement—are bootstrapped (i.e., resampling with replacement, determining mean of each resample, repeating n times) to give a bootstrap sampling distribution of [$CO_{2\ (aq)}$].
3. Conversion to pCO_2: Bootstrapped [$CO_{2\ (aq)}$] values are converted to pCO_2 according to Henry's law.
4. Plotting of bootstrapped pCO_2 values: The bootstrapped pCO_2 values are plotted as boxplots to visualize bootstrap sampling distributions of pCO_2.

To validate this novel approach, we apply it to late Pleistocene (111–258 ka) alkenone ε_p data of ODP site 999 in the Caribbean (Badger et al., 2019). With the diffusive model, these alkenone ε_p data do not reproduce glacial-interglacial variability recorded in ice core records (Badger et al., 2019). However, albeit far from perfect, bootstrapping of core-top and sediment trap data broadly reproduces pCO_2 values consistent with ice core data (Bereiter et al., 2015) (Figure S3 in Supporting Information S1). Culture bootstrapping overestimates pCO_2 during interglacial periods, likely due to the lack of temperature constraints. This implies core-top bootstrapping is a reasonable approach to reconstructing pCO_2 based on alkenones. However, it should be noted that the modern-day ocean has only a limited range of [$CO_{2\ (aq)}$] (Figure S2 in Supporting Information S1) which means the maximal possible pCO_2 reconstruction of the core top method is ~500 µatm.

3.2. Analytical Methodology

3.2.1. Alkenone $\delta^{13}C$

Total lipid extraction from ~5 g of freeze-dried, powdered samples was carried out with Dionex accelerated solvent extraction (ASE 350) or with microwave extraction (MEX) and using a dichloromethane (DCM):MeOH (9:1 v/v) mixture in the GeoLab at Utrecht University. The total lipid extracts (TLE) were dried under a N_2 flow and subsequently separated into three fractions according to polarity. Using activated Al_2O_3 column chromatography yielded an apolar fraction using hexane:DCM (9:1 v/v), a ketone fraction using hexane:DCM (1:1 v/v), and a polar fraction using DCM:MeOH (1:1 v/v), respectively, which were then dried under a N_2 stream. Ketone fractions (n = 20) were diluted with 50 µl Ethyl Acetate and 1 µl was injected onto an Agilent 6890N gas chromatograph (GC), coupled to a flame ionization detector (FID; CP Sil-5 fused silica capillary column, 50 m × 0.32 mm, 0.12 µm film) to test for the presence of $C_{37:2}$ alkenones which were identified based on retention times. Subsequently, 18 ketone fractions that contained sufficient alkenones were injected onto a Thermo Trace 1310 GC (CP Sil-5 column, 25 m × 0.32 mm, 0.12 µm film) coupled to a Thermo Delta V Isotope Ratio Mass Spectrometer (IRMS) at the Royal Netherlands Institute of Sea Research (NIOZ, Netherlands) to

measure the alkenone-specific ($C_{37:2}$) $\delta^{13}C$ values in parts per mill (‰) relative to Vienna Pee Dee Belemnite (VPDB). Mean standard error based on duplicate measurements of single samples was 0.11‰.

3.2.2. Bulk Organic Carbon $\delta^{13}C$

Approximately 1 g of 146 sediment samples was decalcified to measure the isotopic signature of the total organic carbonate; $\delta^{13}C_{TOC}$. Decalcification occurred by treating the powdered sample material three times with 25 ml of 1M HCl at room temperature. Between these treatments, samples were shaken and centrifuged at 2100 RPM and eventually rinsed off with 30 ml Milli-Q. After decalcification the samples were put in an oven at 60°C until dried. For isotopic measurements the samples were finely crushed and approximately 8 mg was measured on a Fison NA 1500 CNS analyzer coupled to a Finnigan Delta Plus IRMS at Utrecht University. Results were calibrated to VPDB using two standards, an inhouse graphite-quartzite (GQ) standard and nicotinamide. Mean reproducibility based on repeated measurements of the GQ standard was 0.03‰.

3.2.3. Dinocyst $\delta^{13}C$

Palynological residues of 11 samples of Wubben et al. (2024), prepared using standard HCl/HF treatment, were washed over a 10 µm-mesh sieve with ultraclean/demineralized water (Milli-Q) and transferred to a glass vial with Milli-Q. Individual *S. ramosus* cysts were picked from a single residue droplet in a glass petri dish with a strung-out glass pipette attached to Narishige IM-9B micro-injector under a Leica inverted microscope following methods as previously described (Frieling et al., 2023; Sluijs et al., 2018). The specimens were picked based on the typical morphological characteristics of *S. ramosus*, as well as a uniform cyst size, process length and color, and contamination of other organic material was minimized. During picking, the dinocysts were first transferred to a separate demineralized water droplet within the same petri dish which was eventually concentrated with as many specimens as possible. Subsequently, the droplet with picked cysts was transferred onto a 6 mm diameter nickel disc which was allowed to dry overnight. Next, another clean nickel disc is added on top of the prepared plate and compressed together at maximum 1 tons of pressure to fixate the cysts to either one of the plates. Before measurement, approximately 1 mm^2 of polyethylene (PE) standard (International Atomic Energy Agency, IAEA, CH-7) is added onto the nickel plate which has a certified $\delta^{13}C$ value of $-32.15 + 0.05$‰.

Stable carbon isotope measurements of the picked dinocysts were carried out according to the procedure previously described in Van Roij et al. (2017) with the laser ablation-nano-combustion-gas-chromatography-isotope ratio mass spectrometry (LA/nC/GC-IRMS) set-up. In this system, dinocysts are exposed to focused ultraviolet laser ablation and resulting small particulate dinocyst fragments are transferred on helium carrier gas into fused-silica capillaries to a combustion oven where they are oxidized. The produced CO_2 is transported to a GC combustion III interface (ThermoFinnigan) and subsequently into an IRMS (Thermo Fisher DeltaV Advantage) for isotope analysis. Carbon isotope data are reported relative to the international Vienna Pee Dee Belemnite (VPDB) carbonate standard. During ablation, the ablation duration, crater size and position, and energy level are continuously monitored to ensure accurate analysis.

Continuous ablation and measurements of the PE standard that is used to align individual isotope measurements of cysts with VPDB in each run ($n = 191$) shows 0.4‰ (98.8%) accuracy and average precision (standard deviation) is 0.3‰. On average 16 dinocyst measurements were performed ($n = 9$–21) for each of the 11 measured samples. Due to their relatively thin cyst wall, multiple (3–5) *S. ramosus* specimens were analyzed simultaneously to guarantee sufficient yield (cumulative m/z 44, 45 and 46 peak area of >0.2 Voltseconds (Vs)) (cf. Frieling et al., 2023). Standard deviation of the isotopic signal significantly increases for yields <0.2 Vs for dinocyst measurements, and average dinocyst $\delta^{13}C$ values seem to divert toward higher values (Figure S7 in Supporting Information S1). This skew could be caused by minor contamination of residual CO_2 in the system, which has an average signature of -26.87 ± 0.08‰ (Van Roij et al., 2017) and using PE standard measurements and endmember mixing was estimated to contribute ~0.04 Vs per measurement (Frieling et al., 2023). Akin to Frieling et al. (2023), we applied a simple isotope endmember mass balance mixing model to correct for skewing at low signal intensities, and 8 measurements were removed before further evaluation. This correction yielded a |0.02‰| and |0.4‰| deviation of the mean sample $\delta^{13}C$ values for PE and *S. ramosus*, respectively, relative to the raw results. Assessment of the data distribution of the individual isotope measurements, following correction for small yields (<0.2 Vs) and outlier removal (±2.5 quartile range), indicates that all samples have a distribution indistinguishable from a normal (gaussian) distribution (Figures S8 and S9 in Supporting Information S1). The

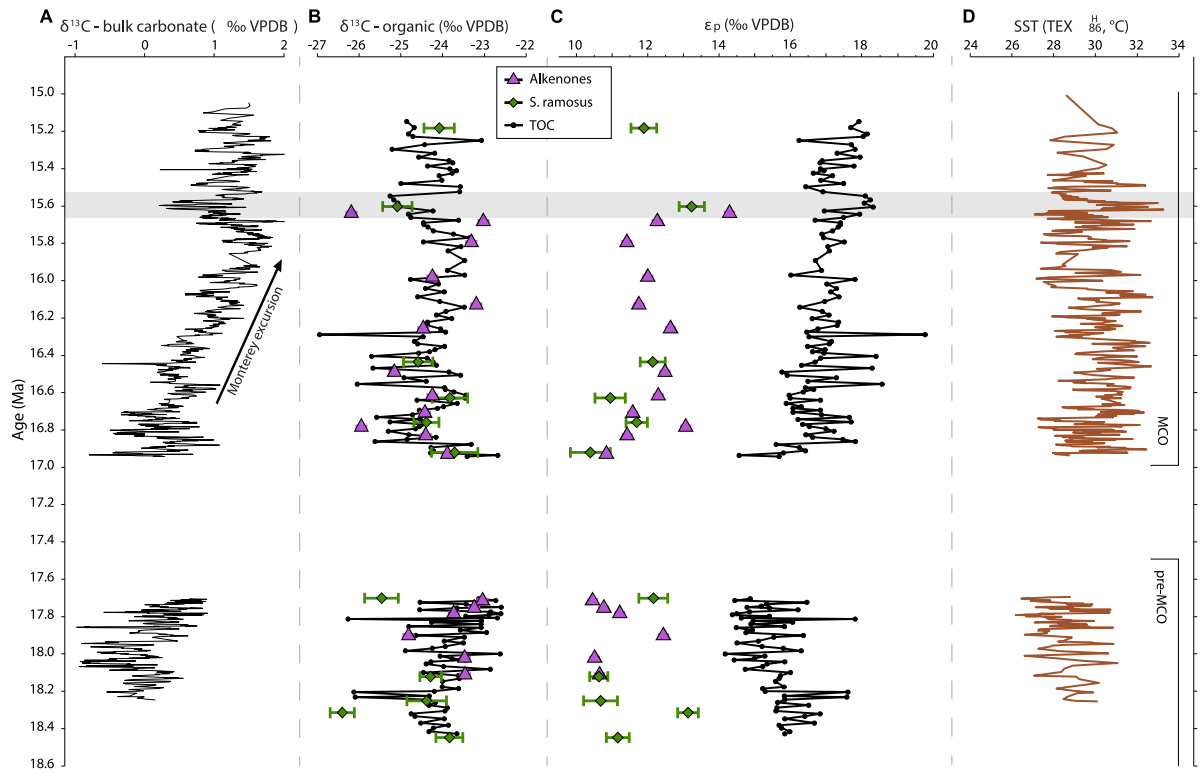

Figure 1. Phytoplankton ^{13}C-fractionation across the Miocene Climatic Optimum onset. (a) Bulk carbonate $\delta^{13}C$ (Wubben et al., 2023), (b) bulk organic carbon $\delta^{13}C$ (black), alkenone $\delta^{13}C$ (purple) and dinocyst *S. ramosus* $\delta^{13}C$ (green). (c) ε_p values based on alkenones and dinocyst *S. ramosus* (top horizontal axis) and based on TOC (bottom horizontal axis; both horizontal axes exhibit same tick marks and dynamic range of values) (d) TEX_{86}^{H}-based sea surface temperature (Wubben et al., 2024). Error bars represent analytical uncertainty based on repeated measurements (b and c) and are smaller than the symbol where not visible.

reconstructed means and standard errors of our *S. ramosus* $\delta^{13}C$ measurements were therefore utilized for ε_p reconstructions.

4. Results

4.1. $\delta^{13}C$ and ε_p

Both $\delta^{13}C_{37:2}$ and $\delta^{13}C_{TOC}$ values show large short-term variability that corresponds to the orbital-scale variability previously recorded in this core material (Spiering et al., 2024). The $\delta^{13}C_{TOC}$ record yields lower average values within the MCO compared to the pre-MCO interval. The two time intervals do not have significantly different $\delta^{13}C_{37:2}$ and $\delta^{13}C_{dino}$ values (Figure 1b; Table 1). The drop or stability in the $\delta^{13}C$ of the organic substrates clearly diverges from the coeval positive Monterey excursion, recorded globally, and locally in bulk carbonate $\delta^{13}C$ (Figure 1a).

As carbonate $\delta^{13}C$ is assumed to reflect the $\delta^{13}C$ of dissolved inorganic carbon (DIC; see methods), the drop from pre-MCO to MCO in $\delta^{13}C$ of the organic phases implies that ε_p values significantly increased across the onset of the MCO by up to 1.5‰ (Figure 1c; Table 1).

Between 16.9 and 16.1 Ma, $\delta^{13}C_{TOC}$ record exhibits two ~400 kyr-long cycles (amplitude ~2.5‰) that also appear in ε_p (amplitude ~0.75‰, Figure S4 in Supporting Information S1). This is corroborated by the lower-resolution $\delta^{13}C_{37:2}$ and $\varepsilon_{p(37:2)}$ records. Peak ε_p values are reached at ~15.6 Ma in alkenones and *S. ramosus*, supported by high $\varepsilon_{p\text{-TOC}}$ values. The consistency between the ε_p records regarding the rise in ε_p values from the pre-MCO interval to the MCO, and peak ε_p values implies that $\delta^{13}C_{TOC}$ is not strongly influenced by the OM composition, and hence likely mainly reflects variability in algal ^{13}C-fractionation.

Table 1
Mean Miocene Climatic Optimum and Pre-MCO Values for the Various Substrates

	MCO mean	sd	Pre MCO mean	sd	Difference MCO versus pre MCO	*p* value (Mann Whitney-*U* test)
$\delta^{13}C$ bulk carbonate (‰)	0.9	0.49	0.1	0.37	0.8	$<2.2e^{-16}$
$\delta^{13}C$ alkenones (‰)	−20.2	1.00	−19.4	0.63	−0.7	0.17
$\delta^{13}C$ TOC (‰)	−24.3	0.67	−23.9	0.82	−0.4	0.0004
$\delta^{13}C$ *S. ramosus* (‰)	−24.5	0.65	−24.7	0.65	0.2	0.85
ε_p alkenones (‰)	12.2	0.91	11.0	0.75	1.2	0.01
ε_p TOC (‰)	16.7	0.77	15.2	0.80	1.4	$<2.2e^{-16}$
ε_p *S. ramosus* (‰)	20.8	0.94	20.6	1.35	0.2	0.57
pCO_2 diffusive TOC (µatm)	501	52	411	41	90	$<2.2e^{-16}$
pCO_2 diffusive alkenones (µatm)	317	25	280	17	37	0.003
pCO_2 culture bootstrap (µatm)	584	95	447	143	137	0.005
pCO_2 core top bootstrap (µatm)	295	57	204	77	91	0.05

Note. sd = standard deviation. Rightmost column represents *p* values from a Mann Whitney-*U* test to assess significance of the difference between pre-MCO and MCO data populations.

4.2. ε_p—Based CO_2 Estimates

Reconstructed CO_2 values using the conventional diffusive model are somewhat lower based on $\varepsilon_{p(37:2)}$ than values based on $\varepsilon_{p\text{-TOC}}$ (Figure 2b). By convention, our $\delta^{13}C_{37:2}$ record was corrected by 4.2‰ for additional fractionation during alkenone biosynthesis prior to $\varepsilon_{p(37:2)}$—CO_2 conversion (Zhang et al., 2013). Recent work has indicated this offset rather comprises 3.9‰ (±0.4, 1σ; Witkowski et al., 2018, 2024) but we for now retain the 4.2 estimate for comparison with previous records. A 3.9‰ offset would lead to ∼5–10 µatm lower CO_2 estimates. This correction equates to a consistent ∼150 µatm drop in CO_2 estimates so that uncorrected $\varepsilon_{p(37:2)}$-based CO_2 estimates would be nearly identical to $\varepsilon_{p\text{-TOC}}$-based estimates (Figures 1b–1d).

All ε_p-based CO_2 records result in a rise in the partial pressure of CO_2, regardless of the applied model. Based on average pre-MCO and MCO values, the diffusive model produces a ∼40 µatm rise for alkenones and ∼90 µatm for bulk marine organic matter. Unfortunately, uncertainties regarding the diffusive model are large but poorly constrained, despite our explicit reconstructions of the b-value. Therefore, these estimates (Figure 2b; Table 1), both for absolute values and magnitudes of change, should be considered with great care. The large range of absolute values and magnitude of change in the bootstrapped core top $\varepsilon_{p(37:2)}$ data (Figure 2b) reflect the limited number of original data (between $n = 95$ and $n = 21$, depending on reconstructed SST). Reconstructed CO_2 values therefore yield quite high uncertainty but average 204 (±77) µatm before the MCO (before 16.9 Ma) and 295 (±57) µatm during the MCO (after 16.9 Ma) (Figure 2c). Also bootstrapped culture $\varepsilon_{p(37:2)}$ data suggest higher values during MCO than before (Figure 2d). If bootstrapped values before and after 16.9 Ma are compared this represents a rise from 447 (±143) to 584 (±95) µatm.

The overlap in bootstrapped CO_2 estimates for the pre-MCO and MCO intervals could suggest that the rise in pCO_2 between the pre-MCO and MCO intervals is not significant. To assess if there is a statistical difference between average pre-MCO and MCO bootstrap means, we perform a Mann-Whitney U test. This indicates that the averages of the bootstrapped MCO pCO_2 values for both the culture data approach and the core top data approach are significantly higher than pre-MCO values. However, our calculations suggest that the magnitude of change was small, roughly between 100 and 150 µatm.

5. Discussion

5.1. Forcings of Long-Term ε_p Variability

5.1.1. Oceanography and pCO_2

Our three ε_p records all show higher average values during the MCO than below the MCO (Table 1). This implies that this increase is not dependent on the analyzed organic substrate and represents an environmental signal. The

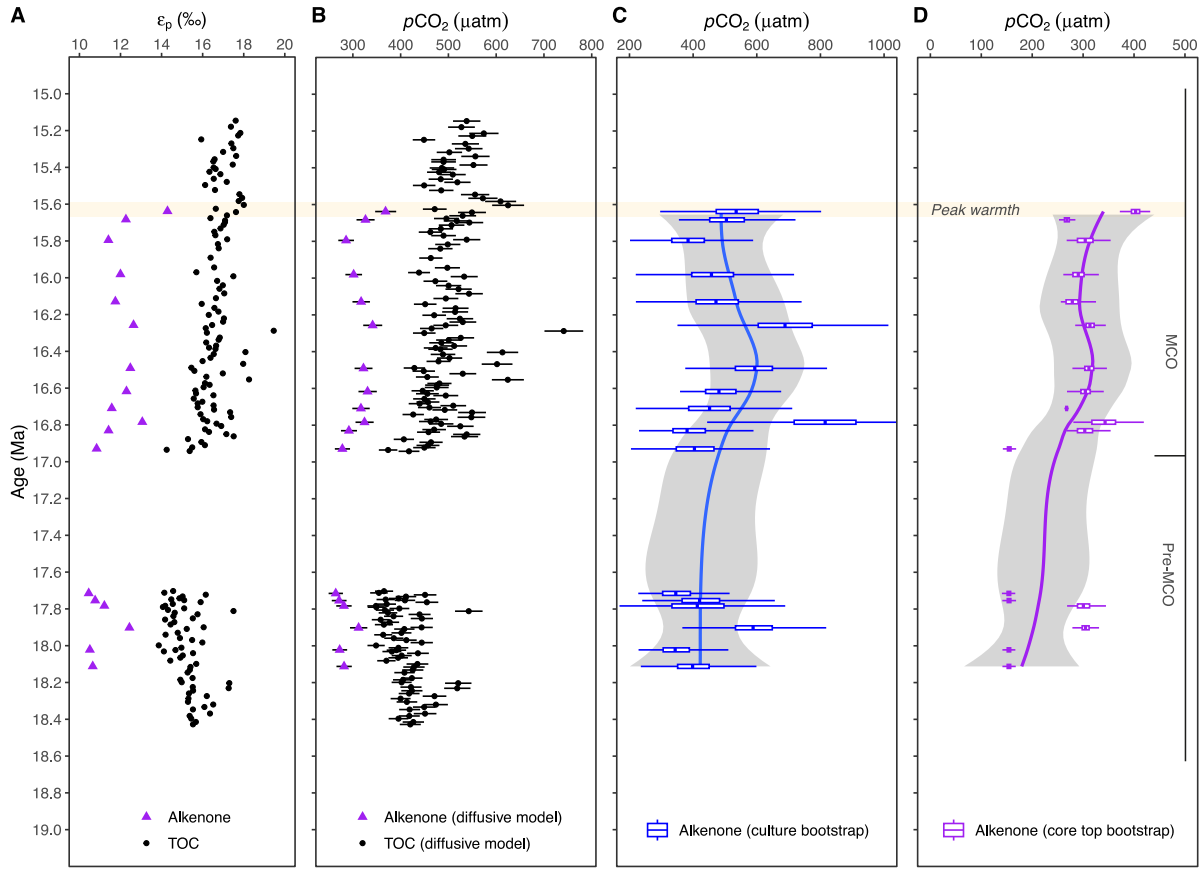

Figure 2. CO_2 reconstructions based on phytoplankton ε_p across the Miocene Climatic Optimum onset. (a) ε_p values based on alkenones and TOC (from Figure 1). (b) CO_2 reconstructions at site 959 based on the diffusive model and $\varepsilon_{p\text{-TOC}}$ (black), and $\varepsilon_{p(37:2)}$ (purple); errors are based on uncertainty in the b-value (see supplementary information). (c) CO_2 reconstructions at site 959 based on the bootstrapped culture data and $\varepsilon_{p(37:2)}$ (d) CO_2 reconstructions at site 959 based on the bootstrapped alkenone core top and sediment trap data and $\varepsilon_{p(37:2)}$. (e) CO_2 reconstructions based on published records from CenCO_2PIP (2023). Data points in (c and d) are standard box-whisker plots of the bootstrap sample mean distributions. The box represents the interquartile range (IQR) between first and third quartile (25th and 75th percentile) and the whiskers extend to 1.5 × the IQR or maximum/minimum values of the data. Solid lines and gray envelopes in (c and d) represent a LOESS fit with standard error, using a span of 0.67.

long-term rise in all three ε_p records is not accompanied by changes in long-term local productivity and upwelling, given published Ba_{bio}, Ti/Al, and dinoflagellate cyst assemblage records (Wubben et al., 2024). On average, we therefore do also not expect major changes in CO_2 equilibration between ocean and atmosphere. It is therefore likely that this trend reflects a change in atmospheric pCO_2.

Upwelling, likely seasonal in nature (Spiering et al., 2024; Wubben et al., 2024), occurred at Site 959 throughout the study interval. Principally, this leads to higher pCO_2 in surface waters and, consequently, organic biomass should yield higher ε_p values. However, if nutrient utilization was complete, pCO_2 in surface waters might have roughly corresponded to the atmosphere. Interestingly, all substrates and models produce rather low pCO_2 values at Site 959 (Figure 2). Values based on the diffusive model and bootstrapped core tops are consistent with published estimates based on alkenones, converted to pCO_2 using the diffusive model (e.g., Super et al., 2018, 2023; Zhang et al., 2013) (Figure 3). Although multiple physiological and environmental factors might have impacted ε_p values, these low values cannot be explained by upwelled CO_2-rich water.

The CO_2 estimates from the diffusive model, both at Site 959 and elsewhere, are lower than published estimates based on foraminifer boron isotope ratios (Figure 3; Table 2) (Greenop et al., 2014; Sosdian et al., 2018, 2023). Analogous to the Pleistocene, we surmise that our and previously published alkenone-based values are affected by environmental factors and physiological processes other than diffusive CO_2 uptake, including light and active bicarbonate uptake (Badger et al., 2019; Phelps, Stoll, et al., 2021; Stoll et al., 2019). Also, the bootstrapped core top alkenone ε_p approach suggests low CO_2 estimates throughout the studied interval, averaging ~265 (±76)

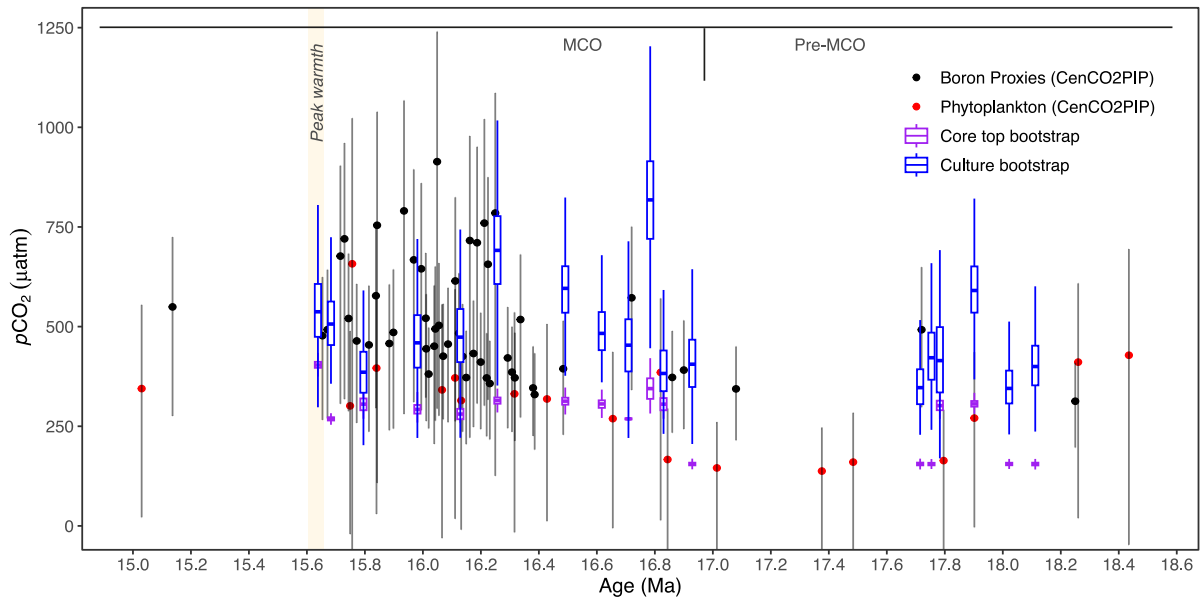

Figure 3. New alkenone-based CO_2 reconstructions compared to published data. CO_2 reconstructions from our two bootstrapped approaches compared to previously published alkenone (red dots) and boron isotope (black dots) estimates. Bootstrap results are all depicted as box-whisker plots of the bootstrap sample mean distributions. The boxes represent the interquartile range (IQR) between first and third quartile (25th and 75th percentile) and the whiskers extend to 1.5 × the IQR.

µatm (Figure 2). However, the core top data set (Phelps, Stoll, et al., 2021) has a bias toward pre-industrial/present-day [$CO_{2\ (aq)}$] (Figure S2 in Supporting Information S1), which hampers reconstructions of pCO_2 concentrations higher than ∼500 µatm. Estimates obtained from the bootstrapped culture data, which has a range of values that allows for reconstructions at higher pCO_2 (Figure S1 in Supporting Information S1), average ∼534 (±159) µatm (Figure 2). Thus, although Pleistocene CO_2 concentrations are best assessed by the bootstrapped core tops, it might be that the culture data provide a more appropriate basis for reconstructing Miocene pCO_2 values. A *t*-test indicates that the bootstrapped culture data produces CO_2 values that are indistinguishable from boron isotope values during the pre-MCO and significantly higher than the boron isotope values in the MCO interval (Figure 3; Table 2), potentially corroborating this notion.

5.1.2. MCO pCO_2 Rise

For alkenones, the diffusive model produces a rise in CO_2 of roughly 40 µatm and for TOC roughly 90 µatm across the onset of the MCO. As indicated above, this method is likely relatively insensitive to pCO_2 variability, notably at relatively low pCO_2 (Badger et al., 2019; Stoll et al., 2019). The bootstrapped data from core tops reproduce Pleistocene glacial-interglacial CO_2 variations much better than the diffusive model (Figure S3 in Supporting Information S1) and suggest a rise of 92 (±91) µatm. However, given the relatively low number of datapoints with high pCO_2 in the core top database (e.g., only 11 datapoints correspond to a pCO_2 of 500 µatm or higher), the increase might be underestimated. The bootstrap approach using culture experiments is not limited by the range of pCO_2 values but strongly overestimates Pleistocene glacial-interglacial variability (Figure S3 in Supporting Information S1). It follows that the somewhat larger rise in pCO_2 values it produces across the onset of the MCO (135 (±213) µatm), might thus represent an overestimate.

Clearly, this result can be improved with expansion of the culture and core top data bases. Notably, targeting regions with naturally occurring high CO_2 concentrations would be of use to improve bootstrapping constraints from core tops. More culturing data points at different temperatures, would contribute to more reined results as well and it might be that the results from both bootstrap methods converge. In any case, at present it shows that two

Table 2
Results of t-Tests Comparing Populations of CO_2 Reconstructions From the Pre-MCO and Miocene Climatic Optimum Intervals, Including Published Boron Isotope Records and Our Alkenone-Based Estimates Using Bootstrapped Culture and Core Top Data

	Pre-MCO	MCO
Boron (pCO_2 ± sd)	374 ± 79	520 ± 143
Culture bs (pCO_2 ± sd)	424 ± 89	520 ± 128
t value boron versus culture	−0.93	−0.004
p value boron versus culture	0.38	1
Core top bs (pCO_2 ± sd)	204 ± 71	295 ± 56
t value boron versus core top	4.3	10.7
p value boron versus core top	0.02	<1e−13

non-parametrical approaches using different data sets that are all based on the same phases and mechanisms of ^{13}C-fractionation result in different reconstructed CO_2 concentrations, which has implications for the uncertainty of the proxy. However, the methods are consistent in that they provide evidence for a ∼100–150 µatm rise in CO_2 concentrations, stemming from a statistically significant difference in the pre-MCO and MCO data populations. If the change in CO_2 would have been larger, we would have expected to see it more clearly in our reconstructions and those based on boron isotopes.

Both absolute values and variability in pCO_2 is poorly defined in the available published data within the interval just before the MCO (CenCO$_2$PIP Consortium, 2023) (Figure 3). The present boron isotope data suggest that pCO_2 values during the MCO were ∼150 µatm higher than during the pre-MCO interval. Our estimate of the magnitude of CO_2 rise is therefore broadly consistent with this. Average pCO_2 values during the MCO averaged ∼500 µatm based on boron isotopes, although variability was remarkably large (Figure 3). A pCO_2 rise of 150 µatm to levels of 500 µatm would explain less than 2°C of global warming given an equilibrium climate sensitivity of 3°C (Sherwood et al., 2020).

A CO_2 rise is traditionally proposed to explain MCO warming and often linked to enhanced volcanic activity related to emplacement of the Columbia River flood basalts and/or increased ocean crust production during the Early Miocene (Herbert et al., 2022; Kasbohm et al., 2023). However, because high CO_2 levels were sustained toward the Middle Miocene (Figures 2 and 3) enhanced volcanic CO_2 degassing would have needed to occur over a longer time-period than has been suggested (∼16.65–15.90 Ma, ∼750 kyr (Kasbohm et al., 2023)). We propose the modest rise in CO_2 across the onset of the MCO may have resulted from imbalances in the carbon cycle of "intermediate" time scale (Sluijs et al., 2013) or redistribution of carbon within the global exogenic carbon cycle (Sosdian et al., 2020).

5.2. Orbital Variability

High-frequency variability on time scales of obliquity and precession occurs in our ε_p throughout the study interval (Figure 1). Aside from long-term lithological changes at Site 959, previous geochemical analyses implied prominent variability in upwelling and productivity forced by obliquity and precession (Spiering et al., 2024; Wubben et al., 2024) (Figure 2). Especially during the early MCO (∼16.9–16 Ma), high amplitude variability in the $\varepsilon_{p(TOC)}$ record on sub-eccentricity timescales correspond to proxy records of export productivity (Ba_{bio}) and dust input (Ti/Al) (Figure 4 and Figure S4 in Supporting Information S1). Perhaps counterintuitively, minima in $\varepsilon_{p(TOC)}$ occur during maxima in biogenic Si (dark brown lithology, Figure 4a), low SST (Figure 3c), and increased Ba_{bio} (Figure 4b) during combined precession minima and obliquity maxima (∼50–60 kyr cycles) throughout the record (Figure 2). These intervals represent episodes of stronger monsoon circulation that drove enhanced upwelling and terrigenous dust influx resulting in lower SSTs and higher productivity (Spiering et al., 2024; Wubben et al., 2024). Possibly, increased nutrient supply through upwelling and dust influx resulted in higher phytoplankton growth rates and decreased ε_p (Burkhardt et al., 1999b). This would also explain the negative relation between productivity (Ba_{bio}) and $\varepsilon_{p(TOC)}$ (Figure S6 in Supporting Information S1). Intensified production should lead to a drop in light availability because of higher concentrations of suspended particulate matter. In culture experiments, reduced light availability causes a drop in ε_p (Rost et al., 2002). Either way, since sub-eccentricity scale variability at Site 959 is so strongly influenced by West African monsoon dynamics and related changes in productivity and water column stratification, the high amplitude ε_p variability should be interpreted in the context of regional oceanographic changes rather than atmospheric pCO_2.

Bandpass filtering of our $\varepsilon_{p(TOC)}$ record suggests 400 kyr eccentricity throughout the MCO (Figure S4 in Supporting Information S1), that is coupled to SST variability (Figure S5 in Supporting Information S1). Especially during the 400-kyr eccentricity maximum at 15.6 Ma, denoted as MCO "peak warming" based on $\delta^{18}O_{benthic}$ (Holbourn et al., 2015), high CO_2 correlates to peak SSTs (Figures 1 and 2). We cannot fully exclude an influence of monsoon intensity on this long eccentricity time scale. However, if it reflects an atmospheric signal, this suggests that insolation variations somehow resulted in the redistribution of carbon between reservoirs during the Early to Middle Miocene, and that this affected atmospheric CO_2, as previously hypothesized (Sosdian et al., 2020), and analogous to the Eocene (Fokkema et al., 2024; Vervoort et al., 2024; Zeebe et al., 2017). The CO_2 and SST peaks in the eccentricity bands correspond to maxima in $\delta^{13}C_{benthic}$, which presumably reflect peaks in organic carbon burial (Kump & Arthur, 1999). This suggests that the orbitally forced variability in organic carbon burial that shaped the $\delta^{13}C$ records was not the dominant control on atmospheric CO_2.

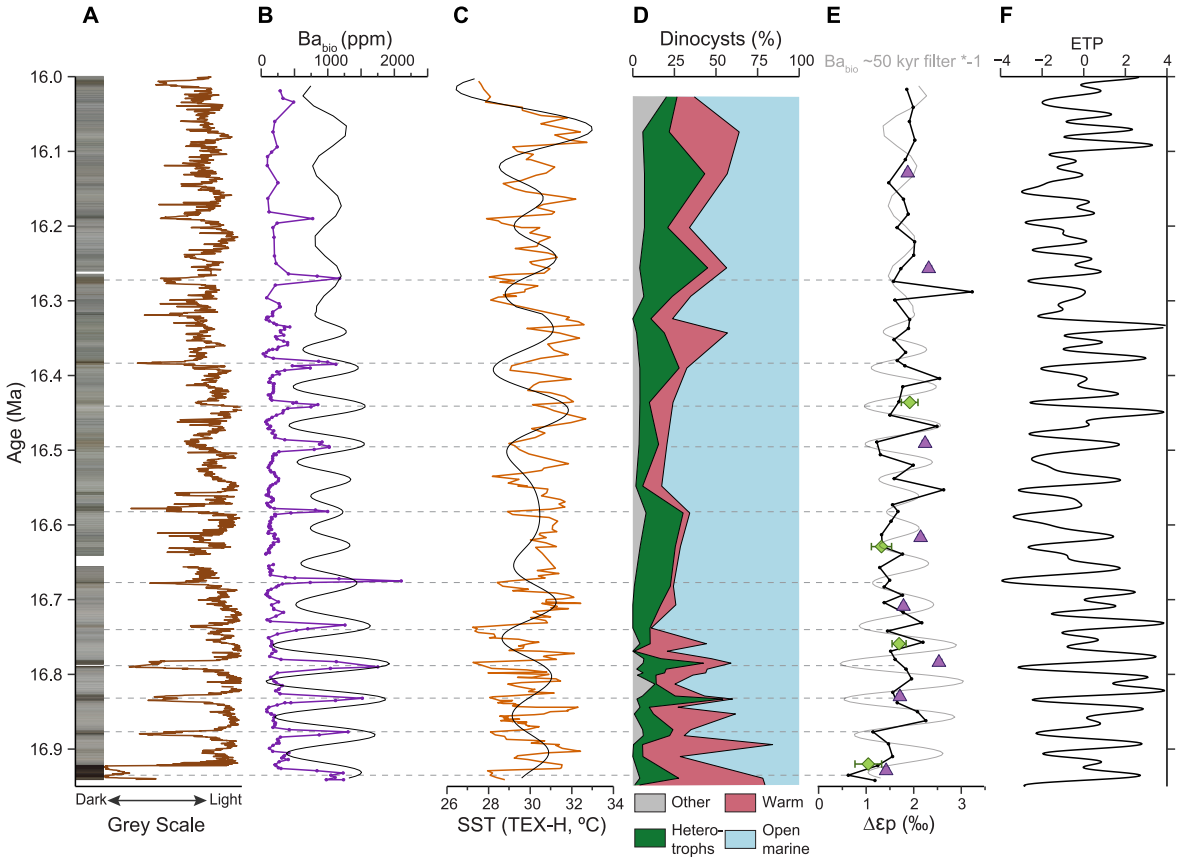

Figure 4. Climatic, biotic and carbon cycle variability during the earliest phase of the Miocene Climatic Optimum (16.95–16 Ma) at Site 959. (a) Lithological column and greyscale (Wubben et al., 2023). (b) Biogenic Ba (purple) and 50–60 kyr filter representative for the precession-obliquity combination tone (Spiering et al., 2024). (c) Sea surface temperature (orange) and 100 kyr eccentricity filter (Wubben et al., 2024). (d) Relative abundance of major dinocyst groups (Wubben et al., 2024). (e) $\varepsilon_{p(TOC)}$ (black), $\varepsilon_{p(37:2)}$ (purple triangles) and ε_p *S. ramosus* (green diamonds) from Figure 1. Mirrored 50–60 kyr Ba_{bio} filter in gray dashed line (Spiering et al., 2024) shows the resemblance of ε_p with $Ba_{bio,}$ notably in the lower part of the record. Error bars as in Figure 1. (f) Eccentricity-Tilt-Precession (ETP) from the orbital solution (Laskar et al., 2004).

6. Conclusions

We present records of ^{13}C-fractionation (ε_p) of bulk marine organic matter, alkenones and the dinoflagellate cyst *Spiniferites ramosus* across the Early to Middle Miocene (18.5–15 Ma) from ODP Site 959. At Site 959, obliquity and precession-scale changes in the West African monsoon and resultant upwelling induced pronounced ε_p variability. However, all records show higher ε_p values during the MCO than the pre-MCO interval that is not associated with long-term changes in local oceanography, suggesting this rise was caused by an increase in atmospheric pCO_2. Through evaluation of multiple methods to convert ε_p to atmospheric pCO_2, including a new statistical approach based on available core top and culture data, we conclude that atmospheric pCO_2 rose only by about 100–150 µatm, consistent with published information.

Conflict of Interest

The authors declare no conflicts of interest relevant to this study.

Availability Statement

All raw data are available from Zenodo (Sluijs et al., 2025).

Acknowledgments
We thank Katrin Hättig and Jort Ossebaar for analytical support at the Royal NIOZ and we extend our gratitude to Desmond Eefting, Klaas Nierop and Helen de Waard for analytical assistance at Utrecht University GeoLab. This study was funded by the European Research Council (ERC) Consolidator Grant 771497 funded by the Horizon 2020 program, awarded to AS, and has benefitted from intellectual contributions by members of the EMBRACER consortium (Summit Grant SUMMIT.1.034), financed by the Netherlands Organization for Scientific Research (NWO). This work was also funded by an award of the Ammodo Foundation to AS, for unfettered research. We thank Timothy Herbert and three anonymous reviewers for their thoughtful comments.

References

Arthur, M. A., Dean, W. E., & Claypool, G. E. (1985). Anomalous ^{13}C enrichment in modern marine organic carbon. *Nature*, *315*(6016), 216–218. https://doi.org/10.1038/315216a0

Badger, M. P. S., Chalk, T. B., Foster, G. L., Bown, P. R., Gibbs, S. J., Sexton, P. F., et al. (2019). Insensitivity of alkenone carbon isotopes to atmospheric CO_2 at low to moderate CO_2 levels. *Climate of the Past*, *15*(2), 539–554. https://doi.org/10.5194/cp-15-539-2019

Badger, M. P. S., Lear, C. H., Pancost, R. D., Foster, G. L., Bailey, T. R., Leng, M. J., & Abels, H. A. (2013). CO_2 drawdown following the middle Miocene expansion of the Antarctic Ice Sheet. *Paleoceanography*, *28*(1), 42–53. https://doi.org/10.1002/palo.20015

Bereiter, B., Eggleston, S., Schmitt, J., Nehrbass-Ahles, C., Stocker, T. F., Fischer, H., et al. (2015). Revision of the EPICA Dome C CO_2 record from 800 to 600 kyr before present. *Geophysical Research Letters*, *42*(2), 542–549. https://doi.org/10.1002/2014GL061957

Bidigare, R. R., Fluegge, A., Freeman, K. H., Hanson, K. L., Hayes, J. M., Hollander, D., et al. (1997). Consistent fractionation of ^{13}C in nature and in the laboratory: Growth-rate effects in some haptophyte algae. *Global Biogeochemical Cycles*, *11*(2), 279–292. https://doi.org/10.1029/96GB03939

Bolton, C. T., & Stoll, H. M. (2013). Late Miocene threshold response of marine algae to carbon dioxide limitation. *Nature*, *500*(7464), 558–562. https://doi.org/10.1038/nature12448

Brandenburg, K. M., Rost, B., Van de Waal, D. B., Hoins, M., & Sluijs, A. (2022). Physiological control on carbon isotope fractionation in marine phytoplankton. *Biogeosciences*, *19*(13), 3305–3315. https://doi.org/10.5194/bg-19-3305-2022

Burkhardt, S., Riebesell, U., & Zondervan, I. (1999a). Effects of growth rate, CO_2 concentration, and cell size on the stable carbon isotope fractionation in marine phytoplankton. *Geochimica et Cosmochimica Acta*, *63*(22), 3729–3741. https://doi.org/10.1016/S0016-7037(99)00217-3

Burkhardt, S., Riebesell, U., & Zondervan, I. (1999b). Stable carbon isotope fractionation by marine phytoplankton in response to daylength, growth rate, and CO_2 availability. *Marine Ecology Progress Series*, *184*, 31–41. https://doi.org/10.3354/meps184031

CenCO2PIP Consortium. (2023). Toward a Cenozoic history of atmospheric CO_2. *Science*, *382*, eadi5177. https://doi.org/10.1126/science.adi5177

Fokkema, C. D., Agterhuis, T., Gerritsma, D., de Goeij, M., Liu, X., de Regt, P., et al. (2024). Polar amplification of orbital-scale climate variability in the early Eocene greenhouse world. *Climate of the Past*, *20*(6), 1303–1325. https://doi.org/10.5194/cp-20-1303-2024

Freeman, K. H., & Hayes, J. M. (1992). Fractionation of carbon isotopes by phytoplankton and estimates of ancient CO_2 levels. *Global Biogeochemical Cycles*, *6*(2), 185–198. https://doi.org/10.1029/92gb00190

Frieling, J., van Roij, L., Kleij, I., Reichart, G. J., & Sluijs, A. (2023). Single-species dinoflagellate cyst carbon isotope fractionation in core-top sediments: Environmental controls, CO_2 dependency and proxy potential. *Biogeosciences*, *20*(22), 4651–4668. https://doi.org/10.5194/bg-20-4651-2023

Greenop, R., Foster, G. L., Wilson, P. A., & Lear, C. H. (2014). Middle Miocene climate instability associated with high-amplitude CO_2 variability. *Paleoceanography*, *29*(9), 845–853. https://doi.org/10.1002/2014PA002653

Herbert, T. D., Dalton, C. A., Liu, Z., Salazar, A., Si, W., & Wilson, D. S. (2022). Tectonic degassing drove global temperature trends since 20 Ma. *Science*, *377*(6601), 116–119. https://doi.org/10.1126/science.abl4353

Hoins, M., Eberlein, T., Van de Waal, D. B., Sluijs, A., Reichart, G.-J., & Rost, B. (2016). CO_2-dependent carbon isotope fractionation in dinoflagellates relates to their inorganic carbon fluxes. *Journal of Experimental Marine Biology and Ecology*, *481*, 9–14. https://doi.org/10.1016/j.jembe.2016.04.001

Hoins, M., Van de Waal, D. B., Eberlein, T., Reichart, G.-J., Rost, B., & Sluijs, A. (2015). Stable carbon isotope fractionation of organic cyst-forming dinoflagellates: Evaluating the potential for a CO_2 proxy. *Geochimica et Cosmochimica Acta*, *160*, 267–276. https://doi.org/10.1016/j.gca.2015.04.001

Holbourn, A., Kuhnt, W., Kochhann, K. G. D., Andersen, N., & Meier, K. J. S. (2015). Global perturbation of the carbon cycle at the onset of the Miocene Climatic Optimum. *Geology*, *43*(2), 123–126. https://doi.org/10.1130/g36317.1

Holbourn, A., Kuhnt, W., Schulz, M., Flores, J.-A., & Andersen, N. (2007). Orbitally-paced climate evolution during the middle Miocene "Monterey" carbon-isotope excursion. *Earth and Planetary Science Letters*, *261*(3–4), 534–550. https://doi.org/10.1016/j.epsl.2007.07.026

Jasper, J. P., & Hayes, J. M. (1990). A carbon isotope record of CO_2 levels during the late Quaternary. *Nature*, *347*, 462–464. https://doi.org/10.1038/347462a0

Kasbohm, J., & Schoene, B. (2018). Rapid eruption of the Columbia River flood basalt and correlation with the mid-Miocene climate optimum. *Science Advances*, *4*(9), eaat8223. https://doi.org/10.1126/sciadv.aat8223

Kasbohm, J., Schoene, B., Mark, D. F., Murray, J., Reidel, S., Szymanowski, D., et al. (2023). Eruption history of the Columbia River Basalt Group constrained by high-precision U-Pb and $^{40}Ar/^{39}Ar$ geochronology. *Earth and Planetary Science Letters*, *617*, 118269. https://doi.org/10.1016/j.epsl.2023.118269

Kump, L. R., & Arthur, M. A. (1999). Interpreting carbon-isotope excursions: Carbonates and organic matter. *Chemical Geology*, *161*(1–3), 181–198. https://doi.org/10.1016/s0009-2541(99)00086-8

Laskar, J., Correia, A. C. M., Gastineau, M., Joutel, F., Levrard, B., & Robutel, P. (2004). Long term evolution and chaotic diffusion of the insolation quantities of Mars. *Icarus*, *170*(2), 343–364. https://doi.org/10.1016/j.icarus.2004.04.005

McClelland, H. L. O., Bruggeman, J., Hermoso, M., & Rickaby, R. E. M. (2017). The origin of carbon isotope vital effects in coccolith calcite. *Nature Communications*, *8*(1), 14511. https://doi.org/10.1038/ncomms14511

Naafs, B. D. A., Castro, J. M., De Gea, G. A., Quijano, M. L., Schmidt, D. N., & Pancost, R. D. (2016). Gradual and sustained carbon dioxide release during Aptian Oceanic Anoxic Event 1a. *Nature Geoscience*, *9*(2), 135–139. https://doi.org/10.1038/ngeo2627

Pagani, M. (2002). The alkenone-CO_2 proxy and ancient atmospheric CO_2. In D. R. Grocke & M. Kucera (Eds.), *Understanding climate change: Proxies, chronology, and ocean-atmosphere interactions* (Vol. 360, pp. 609–632). Philosophical Transactions of the Royal Society of London Series A.

Pearson, A., Polissar, P. J., Carter, S. J., Kocharian, E., Phelps, S. R., Hover, O. D., et al. (2025). Isolating the light dependence of carbon isotope fractionation in *Gephyrocapsa* (*Emiliania*) *huxleyi*. *Geochimica et Cosmochimica Acta*, *408*, 105–115. https://doi.org/10.1016/j.gca.2025.09.033

Phelps, S. R., Hennon, G. M. M., Dyhrman, S. T., Hernández Limón, M. D., Williamson, O. M., & Polissar, P. J. (2021). Carbon isotope fractionation in Noelaerhabdaceae algae in culture and a critical evaluation of the alkenone paleobarometer. *Geochemistry, Geophysics, Geosystems*, *22*(7), e2021GC009657. https://doi.org/10.1029/2021GC009657

Phelps, S. R., Stoll, H. M., Bolton, C. T., Beaufort, L., & Polissar, P. J. (2021). Controls on alkenone carbon isotope fractionation in the modern ocean. *Geochemistry, Geophysics, Geosystems*, *22*(12), e2021GC009658. https://doi.org/10.1029/2021GC009658

Reghellin, D., Coxall, H. K., Dickens, G. R., & Backman, J. (2015). Carbon and oxygen isotopes of bulk carbonate in sediment deposited beneath the eastern equatorial Pacific over the last 8 million years. *Paleoceanography*, *30*(10), 1261–1286. https://doi.org/10.1002/2015PA002825

Riebesell, U., Revill, A. T., Holdsworth, D. G., & Volkman, J. K. (2000). The effects of varying CO_2 concentration on lipid composition and carbon isotope fractionation in *Emiliania huxleyi*. *Geochimica et Cosmochimica Acta*, *64*(24), 4179–4192. https://doi.org/10.1016/S0016-7037(00)00474-9

Rost, B., Richter, K.-U., Riebesell, U., & Hansen, P. J. (2006). Inorganic carbon acquisition in red tide dinoflagellates. *Plant, Cell & Environment*, *29*(5), 810–822. https://doi.org/10.1111/j.1365-3040.2005.01450.x

Rost, B., Riebesell, U., & Sültemeyer, D. (2006). Carbon acquisition of marine phytoplankton: Effect of photoperiod length. *Limnology & Oceanography*, *51*(1), 12–20. https://doi.org/10.4319/lo.2006.51.1.0012

Rost, B., Zondervan, I., & Riebesell, U. (2002). Light-dependent carbon isotope fractionation in the coccolithophorid *Emiliania huxleyi*. *Limnology & Oceanography*, *47*(1), 120–128. https://doi.org/10.4319/lo.2002.47.1.0120

Sherwood, S. C., Webb, M. J., Annan, J. D., Armour, K. C., Forster, P. M., Hargreaves, J. C., et al. (2020). An assessment of Earth's climate sensitivity using multiple lines of evidence. *Reviews of Geophysics*, *58*(4), e2019RG000678. https://doi.org/10.1029/2019RG000678

Sluijs, A., Fokkema, C. D., Agterhuis, T., Gerritsma, D., de Goeij, M., Liu, X., et al. (2025). Ocean Drilling Program Site 959 Datasets [Dataset]. *Zenodo*. https://doi.org/10.5281/zenodo.17104194

Sluijs, A., van Roij, L., Frieling, J., Laks, J., & Reichart, G.-J. (2018). Single-species dinoflagellate cyst carbon isotope ecology across the Paleocene-Eocene Thermal Maximum. *Geology*, *46*(1), 79–82. https://doi.org/10.1130/G39598.1

Sluijs, A., Zeebe, R. E., Bijl, P. K., & Bohaty, S. M. (2013). A middle Eocene carbon cycle conundrum. *Nature Geoscience*, *6*, 429–434. https://doi.org/10.1038/ngeo1807

Sosdian, S. M., Babila, T. L., Greenop, R., Foster, G. L., & Lear, C. H. (2020). Ocean Carbon Storage across the middle Miocene: A new interpretation for the Monterey Event. *Nature Communications*, *11*(1), 134. https://doi.org/10.1038/s41467-019-13792-0

Sosdian, S. M., Greenop, R., Hain, M. P., Foster, G. L., Pearson, P. N., & Lear, C. H. (2018). Constraining the evolution of Neogene ocean carbonate chemistry using the boron isotope pH proxy. *Earth and Planetary Science Letters*, *498*, 362–376. https://doi.org/10.1016/j.epsl.2018.06.017

Spiering, B. R., Wubben, E., Hilgen, F. J., & Sluijs, A. (2024). Early to middle Miocene astronomically paced climate dynamics in the Eastern Equatorial Atlantic. *Paleoceanography and Paleoclimatology*, *39*(5), e2023PA004768. https://doi.org/10.1029/2023PA004768

Steinthorsdottir, M., Coxall, H. K., de Boer, A. M., Huber, M., Barbolini, N., Bradshaw, C. D., et al. (2021). The Miocene: The future of the past. *Paleoceanography and Paleoclimatology*, *36*(4), e2020PA004037. https://doi.org/10.1029/2020PA004037

Steinthorsdottir, M., Jardine, P. E., & Rember, W. C. (2021). Near-future pCO_2 during the hot Miocene climatic optimum. *Paleoceanography and Paleoclimatology*, *36*(1), e2020PA003900. https://doi.org/10.1029/2020PA003900

Stoll, H. M. (2005). Limited range of interspecific vital effects in coccolith stable isotopic records during the Paleocene-Eocene thermal maximum. *Paleoceanography*, *20*(1), PA1007. https://doi.org/10.1029/2004PA001046

Stoll, H. M., Guitian, J., Hernandez-Almeida, I., Mejia, L. M., Phelps, S., Polissar, P., et al. (2019). Upregulation of phytoplankton carbon concentrating mechanisms during low CO_2 glacial periods and implications for the phytoplankton pCO_2 proxy. *Quaternary Science Reviews*, *208*, 1–20. https://doi.org/10.1016/j.quascirev.2019.01.012

Super, J. R., Thomas, E., Pagani, M., Huber, M., O'Brien, C., & Hull, P. M. (2018). North Atlantic temperature and pCO_2 coupling in the early-middle Miocene. *Geology*, *46*(6), 519–522. https://doi.org/10.1130/g40228.1

Van Roij, L., Sluijs, A., Laks, J. J., & Reichart, G.-J. (2017). Stable carbon isotope analyses of nanogram quantities of particulate organic carbon (pollen) with laser ablation nano combustion gas chromatography isotope ratio mass spectrometry. *Rapid Communications in Mass Spectrometry*, *31*(1), 47–58. https://doi.org/10.1002/rcm.7769

Vervoort, P., Kirtland Turner, S., Rochholz, F., & Ridgwell, A. (2024). Earth system model analysis of how astronomical forcing is imprinted onto the marine geological record: The role of the inorganic (carbonate) carbon cycle and feedbacks. *Paleoceanography and Paleoclimatology*, *39*(3), e2023PA004826. https://doi.org/10.1029/2023PA004826

Vincent, E., & Berger, W. H. (1985). Carbon dioxide and polar cooling in the Miocene: The Monterey hypothesis. In E. T. Sundquist & W. S. Broecker (Eds.), *The carbon cycle and atmospheric CO_2: Natural variations Archean to present* (pp. 455–468). American Geophysical Union.

Witkowski, C. R., von der Heydt, A. S., Valdes, P. J., van der Meer, M. T. J., Schouten, S., & Sinninghe Damsté, J. S. (2024). Continuous sterane and phytane $\delta^{13}C$ record reveals a substantial pCO_2 decline since the mid-Miocene. *Nature Communications*, *15*(1), 5192. https://doi.org/10.1038/s41467-024-47676-9

Witkowski, C. R., Weijers, J. W. H., Blais, B., Schouten, S., & Sinninghe Damsté, J. S. (2018). Molecular fossils from phytoplankton reveal secular CO_2 trend over the Phanerozoic. *Science Advances*, *4*(11), eaat4556. https://doi.org/10.1126/sciadv.aat4556

Woodruff, F., & Savin, S. M. (1991). Mid-Miocene isotope stratigraphy in the deep sea: High-resolution correlations, paleoclimatic cycles, and sediment preservation. *Paleoceanography*, *6*, 755–806. https://doi.org/10.1029/91pa02561

Wubben, E., Spiering, B. R., Veenstra, T., Bos, R., Wang, Z., van Dijk, J., et al. (2024). Tropical warming and intensification of the West African Monsoon during the Miocene Climatic Optimum. *Paleoceanography and Paleoclimatology*, *39*(5), e2023PA004767. https://doi.org/10.1029/2023PA004767

Wubben, E., Veenstra, T., Witkowski, J., Raffi, I., Hilgen, F., Bos, R., et al. (2023). Astrochronology of the Miocene Climatic Optimum record from Ocean Drilling Program Site 959 in the eastern equatorial Atlantic. *Newsletters on Stratigraphy*, *56*(4), 457–484. https://doi.org/10.1127/nos/2023/0749

Zeebe, R. E., Westerhold, T., Littler, K., & Zachos, J. C. (2017). Orbital forcing of the Paleocene and Eocene carbon cycle. *Paleoceanography*, *32*(5), 440–465. https://doi.org/10.1002/2016PA003054

Zhang, Y. G., Pagani, M., Liu, Z., Bohaty, S. M., & DeConto, R. (2013). A 40-million-year history of atmospheric CO_2. *Philosophical Transactions of the Royal Society A: Mathematical, Physical and Engineering Sciences*, *371*(2001), 20130096. https://doi.org/10.1098/rsta.2013.0096

References From the Supporting Information

Conte, M. H., Volkman, J. K., & Eglinton, G. (1994). Lipid biomarkers of Haptophyta. In J. C. Green & B. S. C. Leadbeater (Eds.), *The haptophyte algae* (pp. 351–377). Clarendon Press.

Goericke, R., & Fry, B. (1994). Variations of marine plankton $\delta^{13}C$ with latitude, temperature, and dissolved CO_2 in the world ocean. *Global Biogeochemical Cycles*, *8*(1), 85–90. https://doi.org/10.1029/93gb03272

Mook, W. G., Bommerson, J. C., & Staverman, W. H. (1974). Carbon isotope fractionation between dissolved bicarbonate and gaseous carbon dioxide. *Earth and Planetary Science Letters*, *22*(2), 169–176. https://doi.org/10.1016/0012-821x(74)90078-8

Pagani, M., Huber, M., Liu, Z., Bohaty, S. M., Henderiks, J., Sijp, W., et al. (2011). The role of carbon dioxide during the onset of Antarctic glaciation. *Science*, *334*(6060), 1261–1264. https://doi.org/10.1126/science.1203909

Popp, B. N., Takigiku, R., Hayes, J. M., Louda, J. W., & Baker, E. W. (1989). The post-Paleozoic chronology and mechanism of ^{13}C depletion in primary marine organic matter. *American Journal of Science*, *289*(4), 436–454. https://doi.org/10.2475/ajs.289.4.436

Weiss, R. F. (1974). Carbon dioxide in water and seawater: The solubility of a non-ideal gas. *Marine Chemistry*, *2*(3), 203–215. https://doi.org/10.1016/0304-4203(74)90015-2

Zhang, Y. G., Henderiks, J., & Liu, X. (2020). Refining the alkenone-pCO_2 method II: Towards resolving the physiological parameter '*b*'. *Geochimica et Cosmochimica Acta*, *281*, 118–134. https://doi.org/10.1016/j.gca.2020.05.002